HAL open science

Experimental investigation of CH4-air-O2 turbulent swirling flames by Stereo-PIV

T. Boushaki, N. Merlo, S. de Persis, C. Chauveau, I. Gökalp

To cite this version:

T. Boushaki, N. Merlo, S. de Persis, C. Chauveau, I. Gökalp. Experimental investigation of CH4-air-O2 turbulent swirling flames by Stereo-PIV. Experimental Thermal and Fluid Science, 2019, 106, pp.87-99. 10.1016/j.expthermflusci.2019.04.026 . hal-02113606

HAL Id: hal-02113606

https://hal.science/hal-02113606v1

Submitted on 11 Oct 2021

HAL is a multi-disciplinary open access archive for the deposit and dissemination of scientific research documents, whether they are published or not. The documents may come from teaching and research institutions in France or abroad, or from public or private research centers.

L'archive ouverte pluridisciplinaire **HAL**, est destinée au dépôt et à la diffusion de documents scientifiques de niveau recherche, publiés ou non, émanant des établissements d'enseignement et de recherche français ou étrangers, des laboratoires publics ou privés.

Distributed under a Creative Commons Attribution 4.0 International License

Version of Record: https://www.sciencedirect.com/science/article/pii/S0894177718314250
Manuscript_311e6b935c7d031373c61b481fd6a11d

Experimental investigation of CH_4-air-O_2 turbulent swirling flames by Stereo-PIV

T. Boushaki [1,2,*], N. Merlo[1], S. de Persis[1], C. Chauveau[1], I. Gökalp[1]

[1] ICARE CNRS, 1C, Avenue de la Recherche Scientifique, 45071 Orléans, France
[2] University of Orleans, IUT, GTE – 45067 Orléans, France

*Corresponding author's contact information:
Dr. Toufik BOUSHAKI
ICARE, CNRS, 1C, Avenue de la Recherche Scientifique, 45071 Orléans, France
E-mail address: toufik.boushaki@cnrs-orleans.fr

ABSTRACT

This paper presents an investigation of the dynamic characteristics of non-premixed turbulent swirling flames using the stereo-PIV technique. To finely characterize the flow field, experiments are performed in the longitudinal and transverse planes in non-reacting and reacting conditions. The burner configuration studied in this work is a coaxial swirl stabilized burner used in the turbulent regime. The swirler is placed in an annular part supplying the oxidant flow and the central pipe delivers radially a fuel through eight holes symmetrically distributed on the periphery of the tube. The experiments are conducted using a 25 kW parallelepiped combustion chamber, 1 m high and 0.5 m wide, using circulating water as coolant. In the reacting case, the CH_4-air flame is oxygen enriched from 21% to 30% in volume. Effects of the swirl number (0.8 to 1.4) and the global equivalence ratio (0.8 to 1) on the flows topology and structure are analyzed. Results of the present work concern the 3D mean velocity fields, the turbulence intensities, the swirl number measurements and the entrainment rate along the flow. SPIV results show the three-dimensional aspect of the flow including the recirculation zone and the annular zone with swirling jet effects. The comparison between reacting and non-reacting flows shows that the presence of the flame induces a larger radial flow expansion, higher mean velocities and higher turbulence intensities. The results show a bifurcation of the tangential velocity towards the jet central axis by crossing the flame front. It is also shown that the fluctuations of the tangential velocity are mainly responsible for the highest turbulence kinetic energy levels at the top of the central recirculation zone. The entrainment rate of the surrounding gases is measured by stereo-PIV as a function of the swirl number and equivalence ratio. The results explain one possible mechanism for the decrease of the NO_x emissions when the global equivalence ratio increases via an increase of the entrainment rate at the flame base.

Keywords: Turbulent flame, Swirling flame, Oxygen enrichment, Stereo-PIV, CH_4-air

© 2019 published by Elsevier. This manuscript is made available under the Elsevier user license
https://www.elsevier.com/open-access/userlicense/1.0/

1. Introduction

Swirling flows are used as a means of flame control in combustion chambers and have also found application in various types of spray driers and burners [1]. In non-reactive cases, applications include, for example vortex amplifiers and reactors, cyclone separators, vortex shedding from aircraft wings, heat exchangers, jet pumps. In reacting systems, the application of swirl is used mainly as an aid to stabilization of high intensity combustion processes and efficient clean combustion in a variety of practical situations such as gas turbines, industrial furnaces, boilers, gasoline and diesel engines, and many other practical heating devices [2]. Effects of using swirl on flow and combustion are significant and varied, and concern for example: aerodynamics, mixing, flame stability, intensity of combustion, pollutant emissions. While swirl burners are not new to combustion, it is only these last years, in particular by using laser diagnostics, that investigations have been made to understand how and why rotating flows have such significant effects on flows and flames. The present work is a contribution to the understanding of swirling flows and flames in burners. Various benefits of swirling reacting flows are now well-known and studied, such as: the enhancement of flame stabilization due to the vortex breakdown phenomenon, responsible for the central recirculation zone (CRZ) occurrence [3-6], improvement in turbulent mixing of reactants due to the Precessing Vortex Core (PVC) [7-10]. The rotation of jets induces a recirculation zone in the burner center, which allows a dilution by combustion gases and a decrease in flame temperature limiting NOx emissions [11, 12]. Recent studies have been conducted in different aspects of swirling flows. For example, Huang et al. [13] investigated the flow and mixing properties of the swirling double-concentric jets with a control disc at low central jet Reynolds numbers. Jourdaine et al. [14] studied the stabilization of CO_2-diluted premixed swirling CH_4/O_2 flames and CH_4/air flames using a set of optical diagnostics. Benim et al. [15] conducted numerical investigations of turbulent swirling flames in a model gas turbine

combustor, using the CFD code OpenFOAM with the LES approach. Elbaz and Roberts [16] conducted experiments on a non-premixed methane swirling flame performing detailed measurements of the turbulent flow field, gas species concentrations and temperature field, and in particular investigated the effect of the quarl geometry on the flame structure. Khalil and Gupta [17] investigated the colorless distributed combustion (CDC) combustor providing ultra-high combustion intensity, ultra-low pollutant emissions, uniform thermal field and combustion stability. CDC has been examined under both swirling and non-swirling conditions using different injection velocities to seek improved distributed combustion. Orbay et al. [18] presented experiments and numerical simulations of swirling turbulent flows with and without combustion in a laboratory gas turbine combustor, using PIV/LDV measurements and Large Eddy Simulation calculations. This study focused on the characterization of the mean flow structures and on the analysis of the effect of inflow swirl, on the heat release from a premixed natural gas/air combustor. Candel et al. [19] presented a review of some recent progresses on swirling flame dynamics, in particular the presence of acoustic perturbations. They showed that the response of the swirler to incident acoustic perturbations produces a vorticity wave which is convected by the flow. It is also shown that the flame response is characterized by a combination of heat release rate fluctuations generated by the incoming acoustic and convective perturbations. Von Lavante and Yao [20] numerically studied several types of axisymmetric internal configurations to analyze the development of turbulent swirling and non-swirling flows along the axial direction. A numerical algorithm for solving the three-dimensional axisymmetric internal turbulent flows has been developed. Good agreement of the computational and theoretical results of the velocity profiles as well as pressure distributions has been obtained. The injection geometry of the fuel plays a significant role in flame stability as demonstrated by several authors [21, 22]. Milosavljevic et al. [21] were interested in studying lean stability limits of laboratory-scale swirl-stabilized, gas-fired

burners for three quarl geometries, three fuel nozzle arrangements, and two bulk combustion air velocities and quantified the corresponding flame and recirculation zone lengths. Iyogun et al. [22] reported an experimental investigation on the stability of a swirling non-premixed methane flame in a coaxial burner. PIV technique was used to collect data about the interaction of a jet exiting through a central asymmetric fuel nozzle with its surrounding swirling co-airflow. Experiments were performed for both the reacting and the corresponding non-reacting swirling flows. Cozzi et al. [23] recently investigated the initial region of a swirling gas jet using Stereo Particle Image Velocimetry (SPIV) on a model burner with isothermal swirling air jets. Their study aimed to evaluate the local entrainment rate as a function of swirl number and axial distance from the nozzle. The work was also able to identify the presence of vortex breakdown, the central recirculation zone (CRZ) and the precessing vortex core (PVC). In the presence of swirling annular jets and in non-premixed conditions, the radial injection of the fuel induces a better mixing than axial injection close to the burner exit [24, 25]. Note that the configuration used in the present work has a radial fuel injection at the burner exit. Such turbulent swirling lean flames in lean conditions exhibit high sensitivity to combustion instabilities [26, 27]. Oxygen enrichment of the oxidizer is an effective solution to reduce flame instabilities combining more efficient combustion with an extension of flame stability limits [28, 29]. Combining the effects of radial fuel injection, swirling motion and oxygen enrichment are not well understood. Previous experimental studies of these types of turbulent swirling flames were limited to the examination of pollutant emissions, flame temperatures, and heat transfer characteristics [30, 31]. In a recent study [32], we applied the Volumetric V3V 3D3C velocity measurement technique to non-reacting swirling flows with the same burner. The aim was to study the feasibility and capacity of the V3V 3D3C technique to perform velocity measurements in gaseous flows [32]. In this essentially technical work this new method (V3V 3D3C) was applied for the first time to

gaseous flows. Only one flow condition was explored (bulk velocity 4.67 m/s, Re=7531, swirl number Sn =1.4), in the non reactive case. To validate the measurements obtained by the V3V method, a case explored by Stereo-PIV was used for comparison.

The present paper reports an experimental study of a 20 kW swirl burner focusing on its dynamic features in non-reacting and reacting conditions. In previous papers, [29, 33] described an experimental study performed on the same burner to assess the oxygen enrichment effects on flame stability and pollutant emissions. Flame stabilization regimes were first identified for axial and swirling jets with and without oxygen enrichment. Flame lift-off heights were also quantified varying the swirl intensity, the oxygen enrichment rate and the global equivalence ratio. Recently the authors studied numerically the burner by RANS calculations and DDES (Delayed-Detached Eddy) Simulation and good agreements were found in particular for the mean velocity and temperature fields in the combustion chamber [34]. The flame dynamics is investigated in the present work with the stereo-PIV diagnostic, which is relevant for strongly three-dimensional flows. Topologies of the instantaneous and mean flows are investigated in non-reacting and reacting conditions in order to identify the main characteristics of the swirling jet. Turbulent fluctuations are also determined for the two cases. The coupling between the entrainment rate and the flame lift-off height is presented as a possible explanation for the decrease of the NO_x emissions when the global equivalence ratio increases, based on the available literature and the results presented here.

2. Experimental setup and the Stereo-PIV system

The experimental setup consists of the coaxial swirl burner, the combustion chamber and the Stereo-PIV system. Figure 1 shows the burner configuration used in this study and the indication of the three components of velocity (V_r, V_θ, V_z). The burner has a coaxial

configuration with a swirler located in the annular part. The oxidant flow (air or air-O_2) is delivered in the annular part through the swirler to induce the rotation of flow. The swirler is composed of eight vanes with a fixed angle according to the required level flow rotation intensity. The fuel (here CH_4) is delivered in the central tube and injected in the combustion chamber through eight small holes placed in the top of the tube. More details about the burner can be found in the previous works of the authors [32, 38]. The degree of swirl for rotating flows is usually characterized by the non-dimensional swirl number S_n, which represents the ratio of the angular momentum flux G_θ, and the axial momentum flux G_z. times a characteristic distance of the radial dimension R (for example the outlet radius R_b). It is defined as follows:

$$S_n = \frac{G_\theta}{G_x R} \tag{1}$$

In this study, a geometrical swirl number (S_{ng}) is calculated as a function of the different parameters of the burner. The formula (2) reported by Beér and Chigier [1] is used for the present configuration. It is defined as:

$$S_n = \frac{1}{1-\psi} \cdot \left(\frac{1}{2}\right) \cdot \frac{1-(R_h/R)^4}{1-(R_h/R)^2} \tan\alpha_0 \tag{2}$$

where Ψ is the blockage factor and α_0 is the vane angle. R and R_h are nozzle and vane pack hub radii respectively.

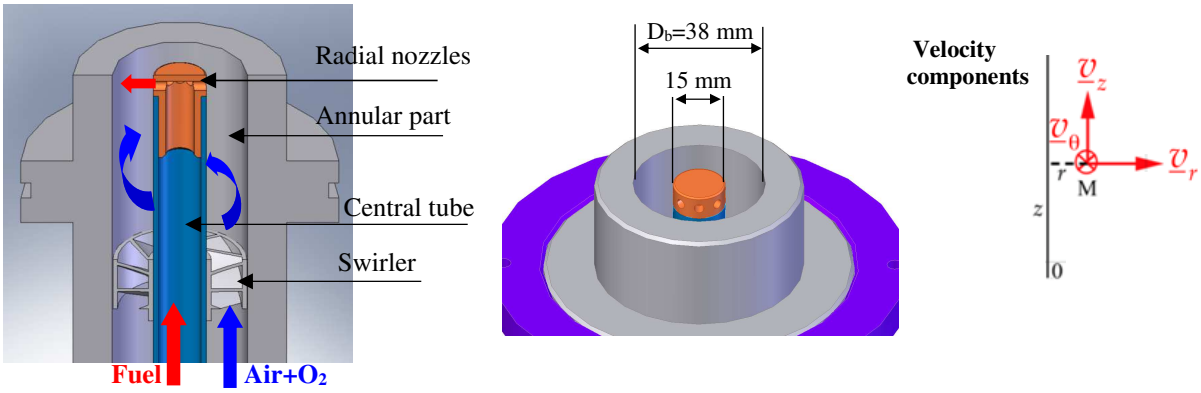

Fig. 1. Schematic view of the swirl burner and indication of velocity components

Three swirl numbers (S_{ng} : 0.8, 1.1 and 1.4) are studied. An oxygen-air mixture is employed as the oxygen-enriched oxidizer flow. Mass flow rates of air, oxygen and fuel are regulated by thermal mass flow controllers. The measurements are performed for oxygen concentrations ranging from 21 to 30 % in volume and for global equivalence ratios of 0.8, 0.9 and 1. Table 1 summarizes the mass flow rates of the reactants as a function of the oxygen enrichment and the equivalence ratio. The Reynolds number in the annular part, based on D_b and the bulk velocity, varies from 7,700 to 8,300. The input power, on a Lower Heating Value (LHV) basis, varies from 12 to 22 kW. The swirling flame is stabilized inside a combustion chamber with a square cross-section of 480 x 480 mm^2 and a height of 1000 mm that is operated at atmospheric pressure.

Table 1 Operating conditions

% O_2 (vol.)	Φ	CH_4 mass flow rate (g/s)	O_2 mass flow rate (g/s)	Air mass flow rate (g/s)
21	0.80	0.24	0	5.2
25		0.29	0.30	5.0
30		0.35	0.70	4.6
21	0.90	0.27	0	5.2
25		0.33	0.30	5.0
30		0.39	0.70	4.6
21	1.0	0.31	0	5.2
25		0.36	0.30	5.0
30		0.44	0.70	4.6

To characterize the flow structure and to analyze the flow dynamic by the three velocity components in the swirl burner, Stereo Particle Image Velocimetry (S-PIV) is used for non-reacting and reacting conditions. Four measurement planes were investigated at the burner exit (Fig.2): one longitudinal plane (LP) and three transverse planes (TP) at z/D_b=0.3, z/D_b=0.8, and z/D_b=1.3. The radial, tangential and axial velocity components, respectively noted (v_r, v_θ, v_z), are illustrated in Fig.1 (c).

A double-pulsed Nd:YAG laser (Minilite 25 mJ/pulse) with a wavelength of 532 nm operating at 10 Hz is used as the light source. An optical system with a plano-convex cylindrical lens (focal length of 12.7 mm) and a spherical lens (focal length of 592 mm) transforms the laser beam into a laser sheet of about 500 µm thickness and about 100 mm height at the center of the measurement window. The laser and the optical system are arranged along the transverse system axis to perform different transverse planes. Synchronization between the cameras and the laser is achieved by means of a TSI synchronizer Laser Pulse 610035. The mean time between two successive frames varies from 20 to 30 µs depending on operating conditions, in order that the maximum displacement of particles does not exceed 1/3 of the laser sheet thickness. The two cameras mounted on Scheimpflug adapters (TSI Powerview Plus 4MP, 12-bit output and 2048 x 2048 pixels^2) are oriented on the same side of the laser sheet. The angle between the two cameras is limited to 30° because of optical access limitations for measurements in the longitudinal measurement plane whereas for the transverse configuration, the angle is up to 60°. Nikon AF Micro-Nikkor 105 mm F/2.8 lenses and band-pass filters centered at 532 nm with a 10 nm bandwidth (50 %) are used to collect Mie particle scattering. A precision-machined twin level calibration target with dot pattern, perfectly centered over the burner inner diameter, is used for calibration. A host computer captures up to 1000 pairs of image frames for each camera

continuously. The laser and the optical system are mounted on a vertical displacement system to allow the realization of transverse planes at different heights (Fig.2.b).

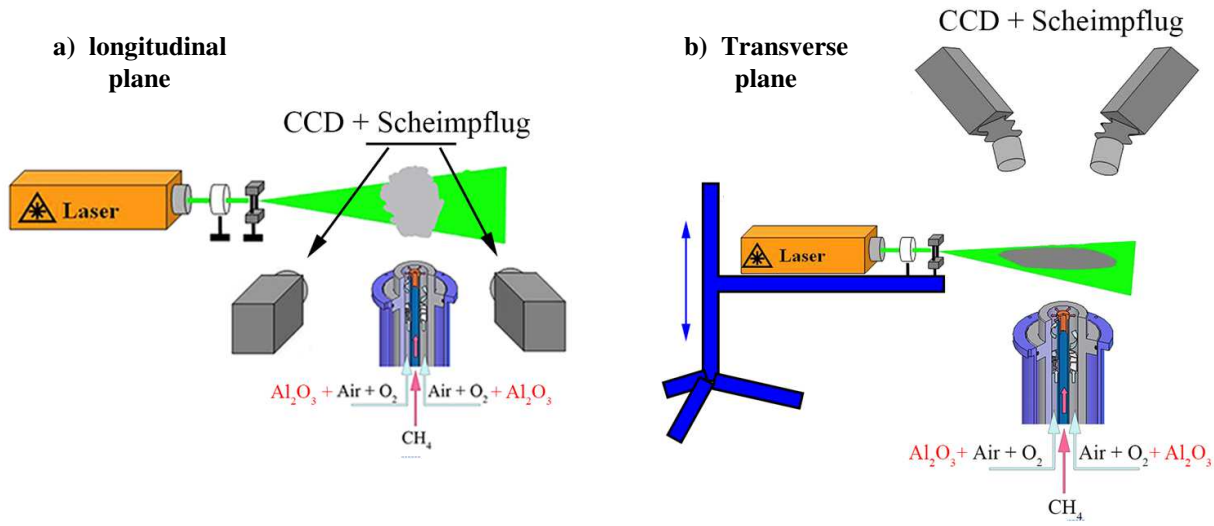

Fig. 2. Arrangement of the cameras for the SPIV system: (a) Configuration for measurements in the longitudinal plane; (b) Configuration for measurements in a transverse plane. The combustion chamber is not shown.

Each frame covers a flow area of about 115 mm (width) x 95 mm (height) for the longitudinal configuration and about 90 mm x 90 mm for the transverse arrangement. TSI Insight 3G software is used to analyze S-PIV images and a background extraction scheme is applied to reacting case images as pre-processing step. The analysis of SPIV images is divided into four steps: 1-Subtracting camera noise and subtracting background noise using minimum intensity detection on a set of shots. 2- Correction of image deformations on PIV images. 3- Analysis of the corrected images of each camera by an intercorrelation method to obtain 2 component velocity fields. 4- Reconstruction of 3-component velocity fields from previously calculated 2 component velocity fields.

Al_2O_3 particles used for seeding the flow are 0.75 µm in diameter. These particles are well suited to high temperature environments with their melting temperature above 2000°C and have a good refractive index of 1.8 for 532 nm. The particles are injected in the flow 2 m before the burner with a cyclone-based seeding system. Al_2O_3 particles are heated at 400°C

before use to avoid the agglomeration problem. Quantity of particles is controlled by valves through the gas flow rate in the line of seeding. The measurements were conducted with seeding rates relatively low in order to not perturb the flow. In addition, the Stokes criterion is checked (St <<1) to ensure that the particles certainly follow the flow. The Stokes number is defined as the ratio between the response time of particles (t_p) and a flow characteristic time (t_f). Considering 32×32 pixels interrogation cells, a magnification ratio of 0.11 and 50 % overlap grid spacing, a typical spatial resolution achieved for the velocity vector grid is 1.1 mm in both directions. The uncertainty in the velocity measurements is mainly related to the uncertainty in the particles displacement since the time between the two laser pulses is known with precision (around a nanosecond for intervals of time around the microsecond in our case). The uncertainty estimation of the displacement is based on the geometric considerations of the configuration implemented in this study. For our experimental configuration, the uncertainty on the actual displacements can reaches to 0.14 pixels in its maximum value, i.e. a maximum displacement about 10 µm. This represents a maximum relative uncertainty in velocity of less than 6 %. The maximum uncertainty of displacement (6% max) corresponds to the maximum displacement (Δx=10 µm) of the particles and therefore to the maximum velocity (V_{max}=9 m/s). For low velocities (e.g. V=1 m/s), the displacement is small (1.5 µm max), and therefore the uncertainty remains low (3.3%).

3. Results and discussion

In Figure 3, samples of the flame issuing from the swirl burner are shown to visualize the general shape of the flame. This flame corresponds to the case with a swirl number S_{ng}=0.8, a global equivalence ratio of Φ=0.8 and with 21, 25 and 30% oxygen concentrations in the oxidant. For these conditions, the flame is lifted and stabilizes at few centimeters (30 to 40 mm) above the burner exit. With the increase of oxygen enrichment rate, the blue zone, which

is considered the heart of the flame (presence of OH* with enough intensity [29]), approaches the burner outlet plane and extends further downstream, since the methane flow rate of increases. It appears that the oxygen enrichment enables to widening the stability range of the flame under the tested conditions. This is most probably linked to an extension of the flammability limits of the CH_4–oxygen enriched air ~~in oxygen~~ mixture. In the 30% O_2 concentration case, a central zone of orange color is observed. This is due, a priori, to enhanced soot emissions or to the chemiluminescence of H_2O which increases with O_2.

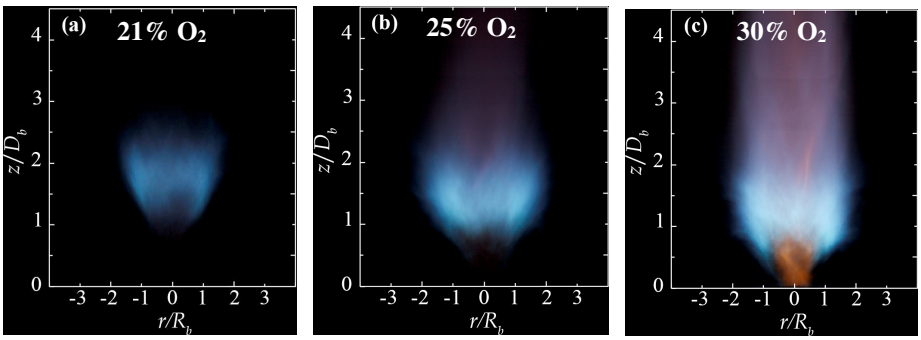

Fig. 3. Samples of flame pictures with varying O_2 enrichment rate for S_{ng}=0.8 and Φ=0.8.

3.1. Global characteristics of mean velocity fields

Mean velocity fields are determined from stereo-PIV measurements performed in non-reacting and reacting cases. The operational conditions are those indicated in Table 1. In non-reacting conditions, N_2 is used instead of CH_4 but the N_2 flow rate is adjusted to keep an equivalent momentum flux at the exit of the fuel injection holes. Figures 4 and 5 show the mean fields of axial (v_z) and tangential (v_θ) velocities for non-reacting and reacting conditions for Φ=0.8; S_{ng}=1.4 and 21% O_2. A longitudinal plane in the center of the burner and three transverse planes at Z/D_b= 0.3, 0.8 and 1.3 are plotted in these figures. Figure 4 illustrates clearly the swirling jet (SJ) and the central reaction zone through the axial velocity (Fig.4.a.b). A recirculation zone appears in the center of flow where the longitudinal velocity is negative. This CRZ is due to the swirl effect and the presence of the central tube in the burner. In

reacting conditions, the maximum tangential velocity is shifted toward the jet central axis. This shift occurs when z/D_b equals to or greater than 0.9 which corresponds to the flame lift-off height determined by OH* chemiluminescence as reported in [28].

We can note that the presence of the flame leads to a widening of the jet in particular in the recirculation zone. The latter becomes more intense with the combustion and tends towards a more pronounced axial symmetry than in the non-reactive case. The presence of the flame seems to induce an increase in the axial velocity downstream of the flow due to gas expansion. These results are also reported in the literature as by Takaji et al [40] and Boushaki et al [41] by comparison between non-reacting and reacting flow as well. Figure 5 shows that the tangential velocity is relatively high since its value varies between 4 and -4 m/s. This is expected because of the helical flow induced by the swirler. The swirled flow invades the entire jet including the CRZ with the presence of the flame. The radial component of the velocity obtained form a combination of four stereo-PIV measurement fields is difficult to exploit qualitatively in a reconstructed 3D form and not presented in this paper.

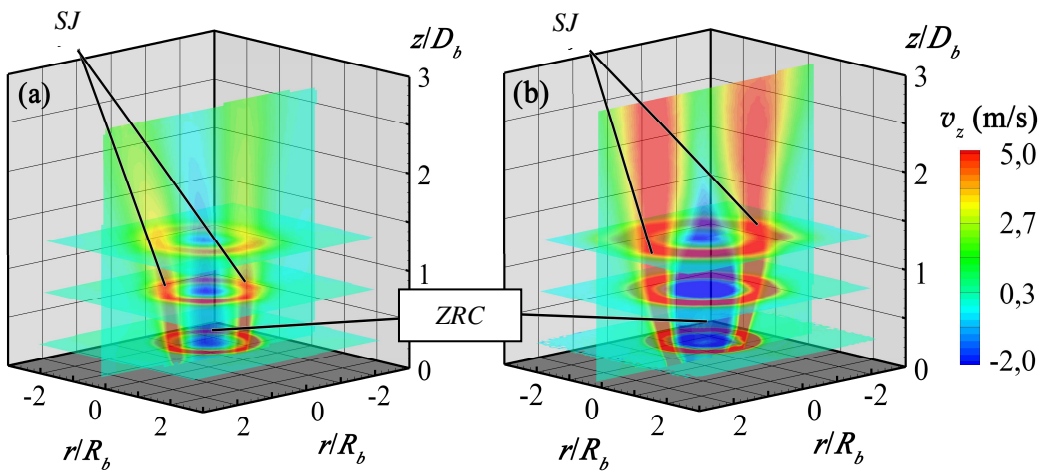

Fig. 4. 3D mean velocity fields of axial velocity v_z as a function of R_b and z/D_b for Φ=0.8; S_{ng}=1.4, 21% of O_2, a) non-reacting flow, b) reacting flow. SJ is the Swirling Jet (SJ) and CRZ is the Central Recirculation Zone (CRZ).

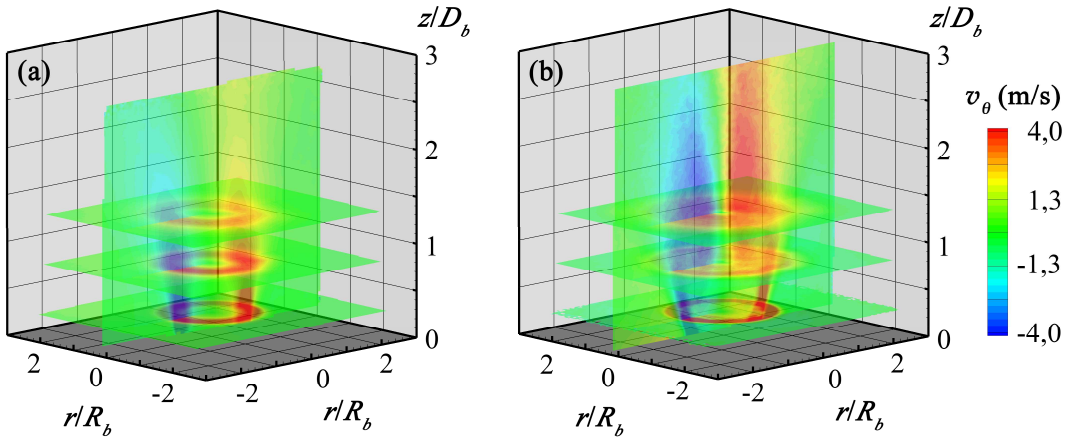

Fig. 5. 3D mean velocity fields of tangential velocity v_θ as a function of R_b and z/D_b for Φ=0.8; S_{ng}=1.4, 21% of O_2, a) non-reacting flow, b) reacting flow.

The transverse planes of the flow field allow completing the information provided in Figures 4 and 5 in particular concerning the variation of the tangential velocity. Figure 6 shows three transverse planes at Z/D_b=0.3, 0.8 and 1.3. The non-reactive and reactive cases (NR and R) are juxtaposed in these figures as a mirror to facilitate direct comparisons between them.

The difference in the size of recirculation zone is clearly visible between the two cases. Typically, at Z/D_b= 0.8, the radius of the recirculation zone, defined by the iso-contour of zero axial velocity, is doubled with the presence of the flame. The acceleration of the flow in the axial direction as indicated by the vectors in Figure 4 is also found close to the burner. A deviation of velocity vectors is observed according to the radial position in the reactive case. This can be explained via a generalized volume expansion of flame which raises globally the temperature of flow before the reaction front.

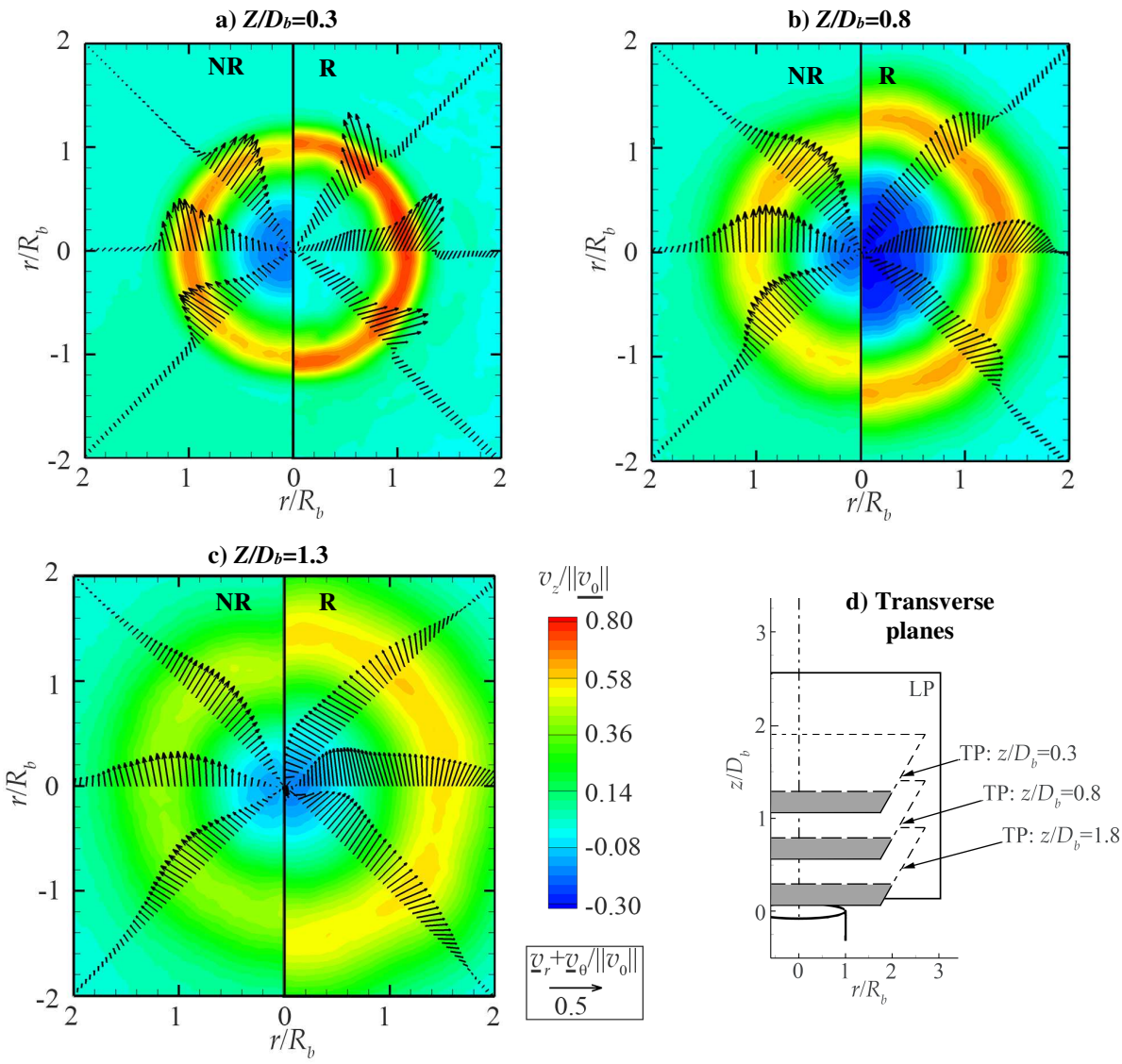

Fig. 6. Contours of normalized axial velocity (level of color) for reacting (right) and non-reacting (left) flows in three transverse planes, Z/D_b: 0.3, 0.8 and 1.3 depicted on Fig6.d for Φ=0.8, S_{ng}=1.4 and 21% O_2. The velocity vectors (in black color) are obtained from the radial and tangential normalized velocity, $\|\upsilon_0\|$= 9.3 and 10.5 m/s in non-reactive and reactive cases, respectively.

3.2. Turbulence intensities

The turbulence levels of the swirling flow are analyzed using the turbulent kinetic energy (k) and the turbulence intensities (q_i) defined respectively as follows:

$$k^{1/2}/\|\underline{v_0}\| = \frac{\sqrt{\frac{1}{2}\left(v_r'^2 + v_\theta'^2 + v_z'^2\right)}}{\|\underline{v_0}\|} \tag{3}$$

$$q_r = \frac{v_r'}{\|\underline{v_0}\|}\ ,\ \ q_\theta = \frac{v_\theta'}{\|\underline{v_0}\|}\ ,\ \ q_z = \frac{v_z'}{\|\underline{v_0}\|} \tag{4}$$

where $\|v_0\|$ is the norm of the velocity vector determined from the average field (from stereo-PIV measurements) for which V_Z (axial velocity) is maximum near the burner exit section.

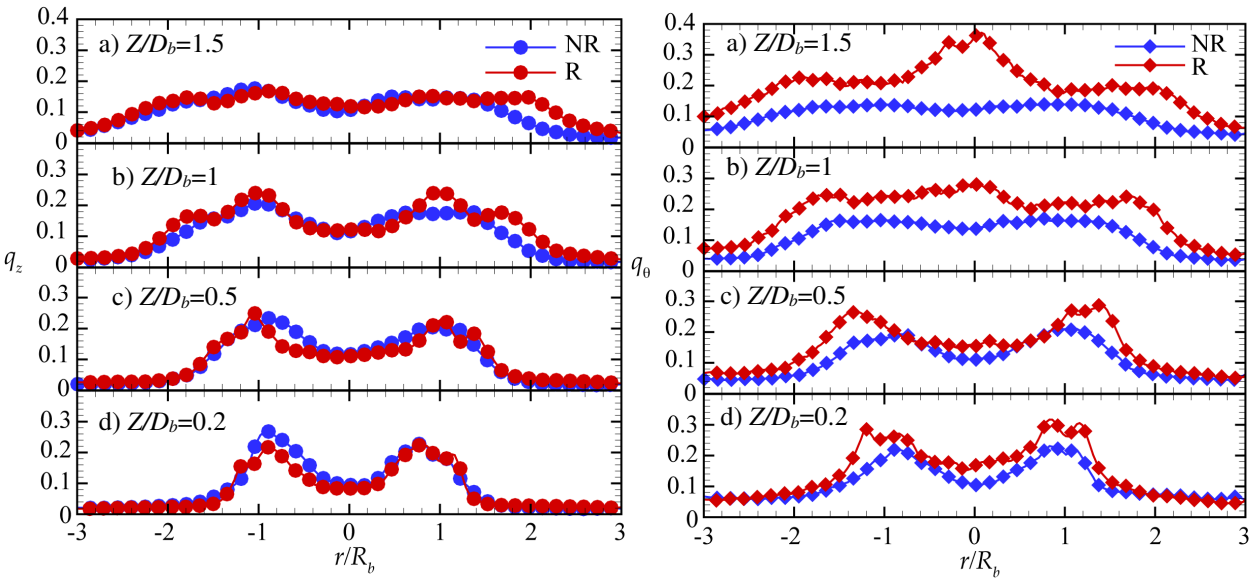

Fig. 7. Radial profiles of the axial (q_z, on the left) and tangential (q_θ, on the right) turbulence intensities for non-reacting (blue lines) and reacting (red lines) conditions for Φ=0.8, S_{ng}=1.4, 21% of O_2 at different z/D_b positions: (a) z/D_b=1.5; (b) z/D_b=1; (c) z/D_b=0.5; (d) z/D_b=0.2.

Figure 7 shows radial profiles of the axial (q_z) and tangential (q_θ) turbulence intensity for non-reacting (NR) and reacting (R) flows. These profiles are plotted for Φ=0.8, S_{ng}=1.4 and 21% O_2 conditions at four z/D_b positions 1.5,1, 0.5 and 0.2. Close to the burner, the two turbulence intensities (q_z, q_θ) have equivalent contributions. The turbulence intensity (q_r), not represented here, is relatively weaker. Profiles of the turbulence intensities ~~rates~~ at this zone indicate a weakly turbulent central region and an annular zone with higher intensities. The central zone is associated with CRZ which returns the flow to the stagnation point imposed by the bluff body. The annular region corresponds to the swirled jet (JS). Further downstream, the profiles flatten and widen, indicating a progressive extending of the turbulence throughout

the jet in the non-reactive case. Combustion changes this general trend. The tangential component fluctuations of the turbulence intensity are amplified by the presence of the flame. For Z/D_b=1.5 and r/D_b= 0, q_θ is multiplied by 4 in the presence of flame which generates turbulence via the fluctuations of the tangential velocity component. This is to be related to the bifurcation of this component towards the jet axis in reactive cases. It appears that the fluctuations of the axial velocity in non-reacting and in reacting flow are of the same order of magnitude.

The transverse fields of the normalized turbulent kinetic energy enable to observe the angular distribution of this quantity, which is absent from the longitudinal planes as illustrated in Figure 8. The spatial distribution and the values of $k^{1/2}/\|\upsilon_0\|$ are consistent with the results in Figure 7. In reacting conditions, turbulence intensity, estimated via the normalized turbulence intensity, reaches higher levels in the jet central axis compared to the non-reacting jet case.

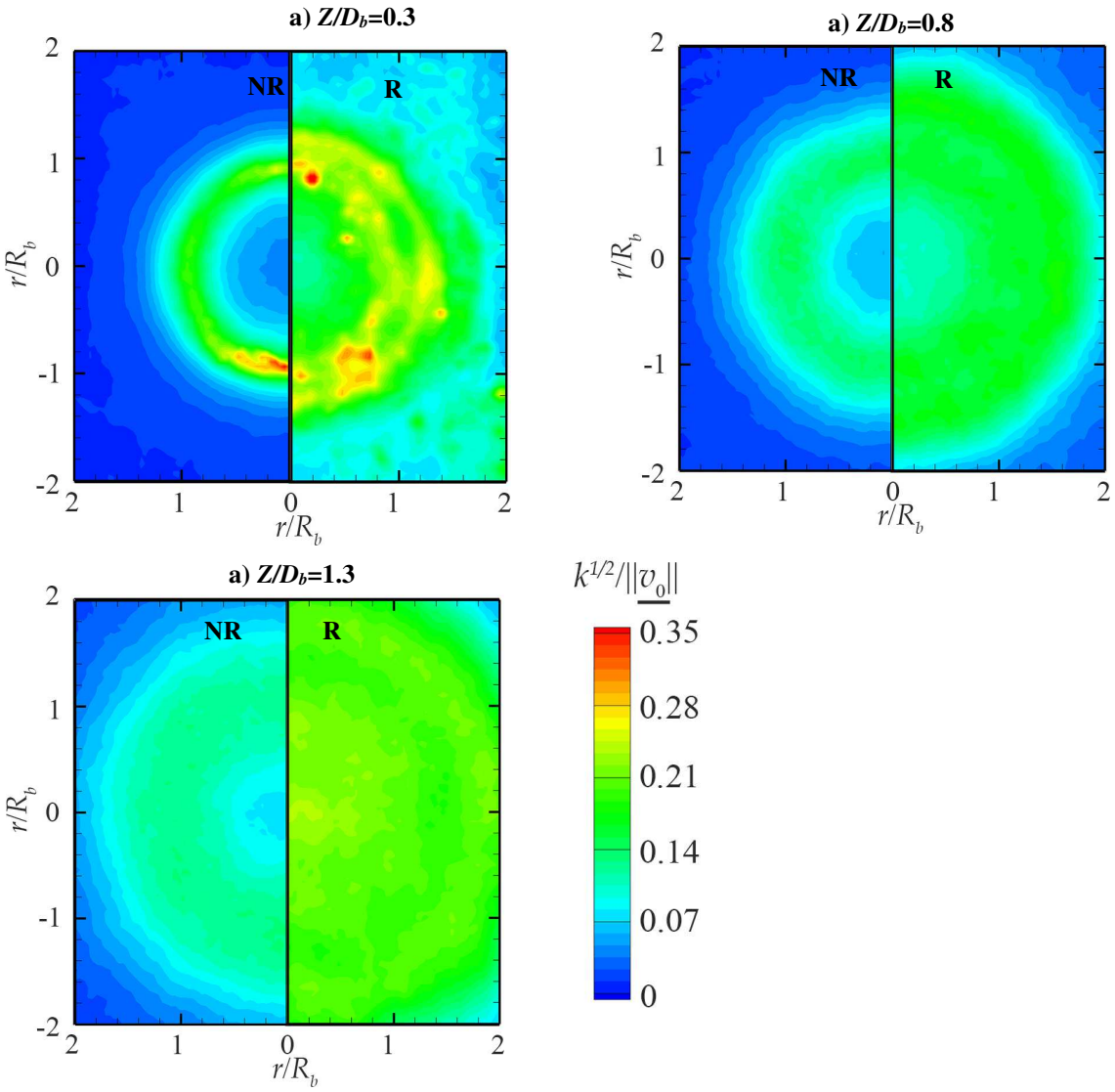

Fig. 8. Contours of the normalized kinetic energy $k^{1/2}/\|v_0\|$ for reacting (R, on the right) and non-reacting (NR, on the left) flows in three transverse planes (Z/D_b: 0.3, 0.8 and 1.3) for the case Φ=0.8, S_{ng}=1.4 and 21% O_2.

3.3. Velocity decay rates

Figure 9 illustrates the influence of combustion on the velocity decay rates by considering the case of S_{ng} = 1.4, Φ = 0.8 and 21% O_2. The symbols in black refer to the maxima of axial velocities in absolute value. The symbols in white refer to the maxima of tangential velocity in absolute value. The squares are used for the left branch, the circles for the right branch and the triangles for the central branch of the flow. The profiles of the velocity decay rates are

presented together in Figure 10 in reactive (R) and non-reactive (NR) conditions. Figure 10.a shows the distribution of normalized axial velocity in the left (LB) and right branch (RB) of the flow. Figure 10.b shows the distribution of normalized axial velocity in the central branch (CB) with its two sides, left (CB_l) and right (CB_r) for the reacting flow. We note that V_{z0} is a maximum velocity obtained closest to the burner exit section. The negative value in Fig.10b is due to V_z (absolute value) because it is in the central zone affected by the CRZ.

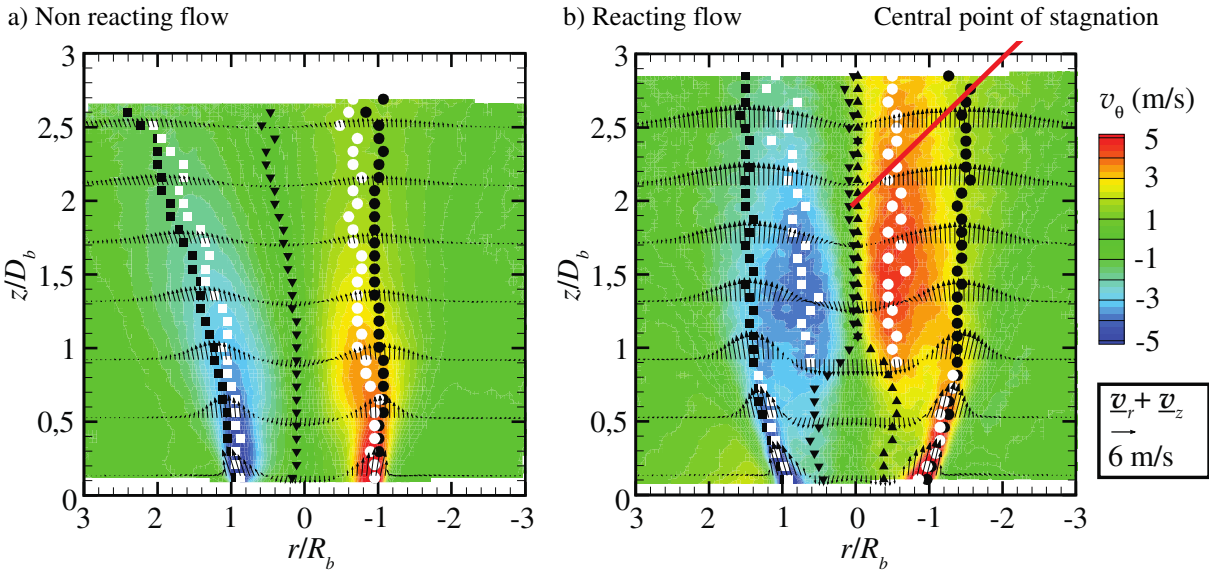

Fig. 9. Velocity decay in non-reacting (a) and reacting flow (b) for the case Φ=0.8, S_{ng}=1.4, 21% of O_2. Symbols locate the maximum velocity of the left branch (■), the right branch (•) and the central branch (▼▲). The black symbols correspond to the axial velocity and the white ones to the tangential velocity.

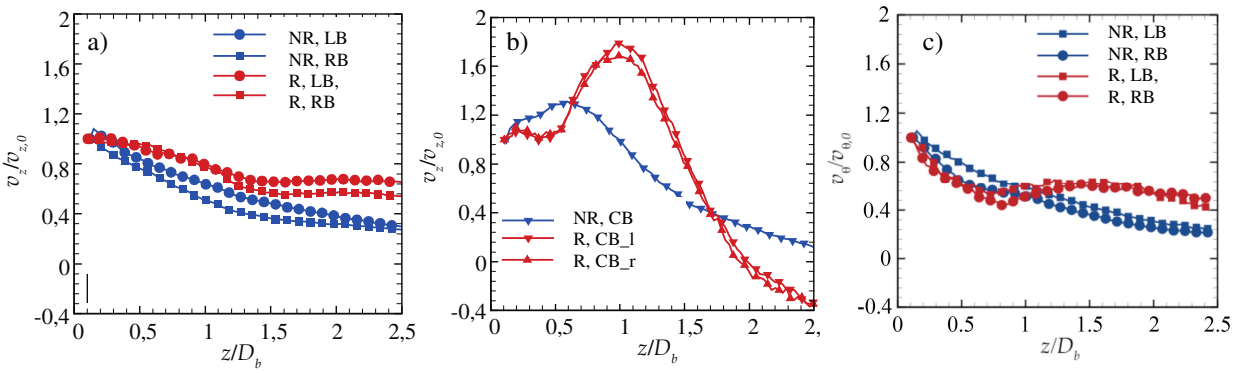

Fig. 10. Axial decay of normalized velocity for the left branch of flow (LB), central branch (CB_l and CB_r) and right branch (RB) for the case S_{ng}= 1,4 et Φ = 0,8, 21 % O_2: (a) axial velocity LB and RB; (b) axial velocity CB_l and CB_r; (c) tangential velocity LB and RB.

In reacting flows, the axial velocity in the swirled jet decreases up to 1.25 D_b (Fig. 10.a), and is stays almost constant due to the presence of the flame and to the expansion of hot gases. In the central axis of CRZ, the maximum axial velocity occurs at Z=1 D_b as shown in Figure 10.b. In the direction of CRZ flow (z= 2.5 to z= 0), the axial velocity increases 1.8 times near the burner and then decreases to stabilize around 0.6 D_b. The non-reactive case displays a velocity maximum close to 1.3 times the velocity of recirculation near the burner. In the non-reactive case, the CRZ has a maximum axial velocity, which is located on the jet axis. In the reactive case, the evolution of profiles is substantially different. At the CRZ top region, the axial velocity profile is parabolic. When Z/D_b decreases, the profile is deformed and exhibits an axial velocity defect in the axis of the jet, which by conservation of mass, results in a slight peripheral over velocity. Besides, Figure 9 shows that for $Z/D_b \leq 1$, two maxima for the axial velocity are distinguished in the CRZ. These latter belong to two distinct branches named CB_l (for the left central branch) and CB_r (for the right center branch), which merge before reaching the central stagnation point. This point is defined by the cancellation of the axial velocity at the flow center as indicated in Figure 9.b. The location of tangential velocity maxima demonstrates the bifurcation of the latter to the axis for $Z=0.8\ D_b$ in the reacting flow. The decrease in tangential velocities is similar in reactive and non-reactive cases up to Z=0.8 D_b. From z= 1 D_b, the tangential velocity in reacting flow increases weakly up to Z= 1.6 D_b and then decreases slightly up to Z= 2.5 D_b. In non-reacting flows, the tangential velocity decay has a classical evolution along the flow

3.4. Evolution of the swirl number

This section describes the evolution of the measured effective swirl number S_n, with z and compares it with the geometrical swirl number S_{ng} determined by the Equation (2). Figure 11 shows the measured swirl number S_n along the flow with the geometrical swirl number S_{ng} in

reacting and non-reacting flow for Φ=0.9 and 21% O_2. The S_n values are calculated by the following formula of Chigier and Chervinsky [35]:

$$S_{n,CC} = \frac{\int_{r_1}^{r_2} \rho(v_\theta v_z + v'_\theta v'_z) r^2 \, \mathrm{d}r}{(r_2 - r_1) \int_{r_1}^{r_2} \rho[v_z^2 - \frac{1}{2} v_\theta^2 + v_z'^2 - \frac{1}{2}(v_\theta'^2 + v_r'^2)] r \, \mathrm{d}r} \tag{5}$$

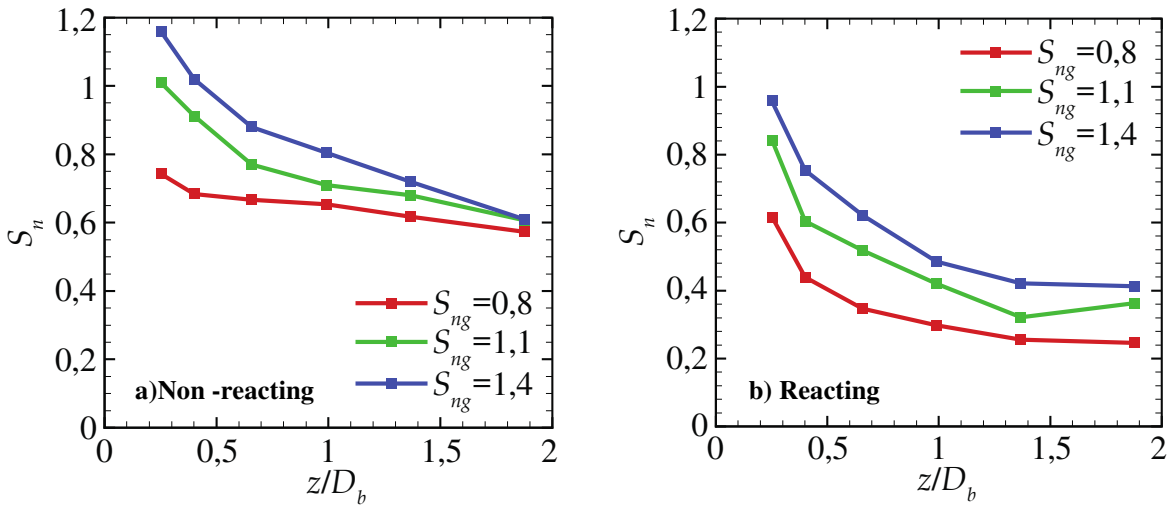

Fig. 11. Measured swirl number S_n along the flow compared with the geometrical swirl number S_{ng} for the case Φ=0.9 and 21% O_2: a) non-reacting flow, b) reacting flow.

r_1 and r_2 rays are determined when the axial velocity of the flow (internal and external of the annular part) is zero for a given z. These integration rays are chosen to correspond to those used in the Beér and Chigier formulas where the axial velocity is zero because of the walls. The equation uses mean axial and tangential velocity profiles obtained by SPIV. The integrals are computed numerically by the 1 mm constant pitch trapezoid method with a pre-polynomial fit of the profiles. The accuracy of the method at order 6 for a S_n value is estimated to be ± 3%.

In the non-reactive case, Figure 11.a shows that the effective swirl number is systematically less than the geometrical swirl number close to the burner outlet as also found by Durox et al. [36]. By extrapolation, it follows that the value of the measured swirl number approaches that of the geometrical swirl number in the vicinity of the burner outlet. The

expansion of the jet at the burner outlet induces a decrease in the momentum of the tangential movement greater than that of the axial movement when z increases, as shown in Figure 12. This results in a decrease in the effective swirl number when z increases. In reacting flow, the presence of the flame tends to decrease the swirl number as shown in Figure 11.b as compared to the non-reacting flow case. This is explained not by the decrease of the tangential momentum but by the increase of the axial momentum due to the acceleration of gases.

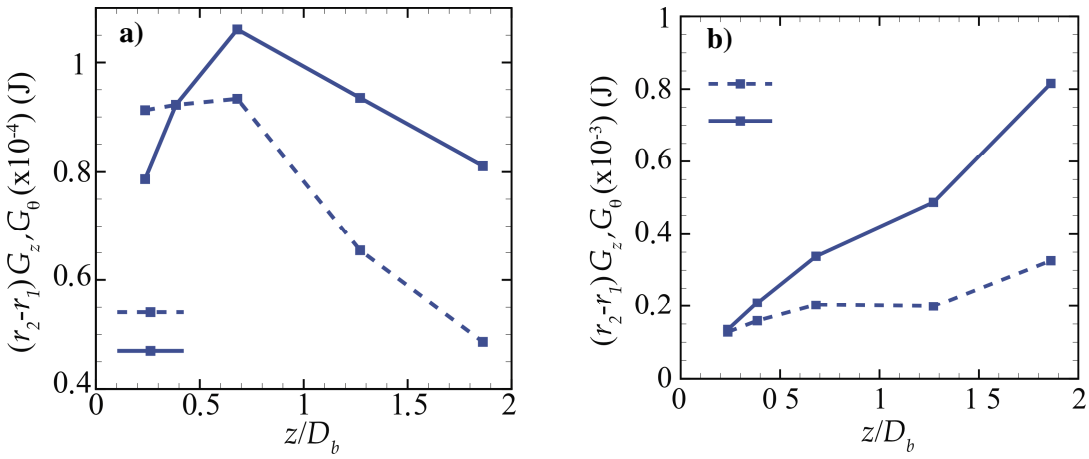

Figure 12. Evolution of axial (G_x) and tangential (G_θ) momentum as a function of z/D_b for S_{ng} = 1.4: () nonreactive case; (b) reactive case: Φ = 0.9; 21% O_2.

3.5. Entrainment rate

The study of the gas entrainment by a diffusion flame or partially premixed flame makes it possible to evaluate the importance of the dilution of initial mixtures by the external medium before the flame front. Figure 13 shows the variation of the entrainment rate (ψ) for the non-reacting flow along the flow axis with the effects of the swirl number in (13.a) and the air flow rate in (13.b).

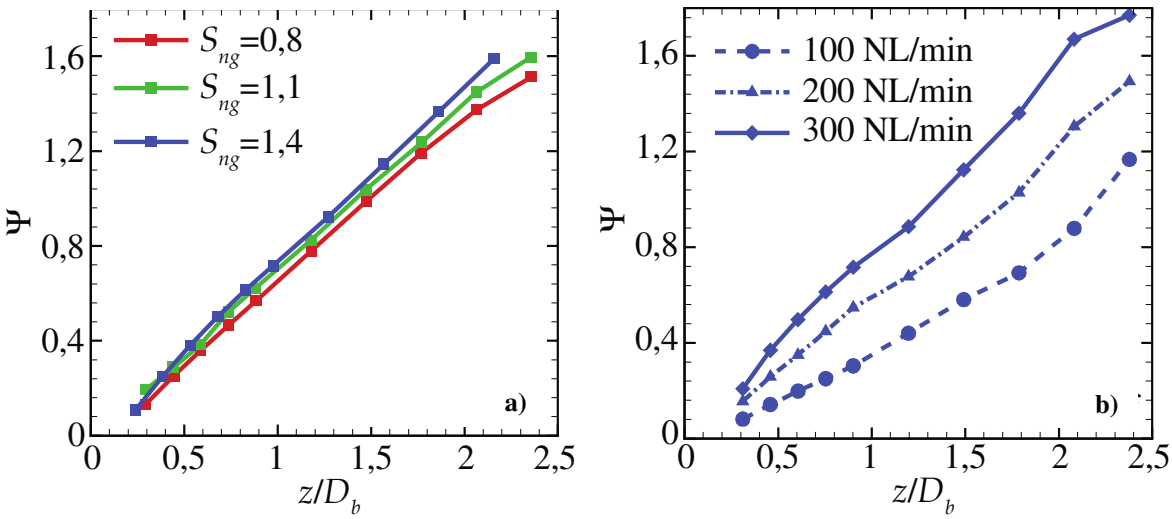

Fig. 13. Entrainment rate (ψ) as a function of z/D_b for the non-reacting flow: a) Effect of swirl number (0.8, 1.1 and 1.4), b) Effect of flow rate of air (100, 200 and 300 Nl/min).

The entrainment rate ψ is defined as the ratio of the entrained mass flow rate Me(z) to the mass flow at injection M_0:

$$\Psi = \frac{M_e(z)}{M_0} = \frac{2\pi\rho \int_0^z R(z)\, v_r(R(z), z)\, \mathrm{d}z}{M_0} \tag{6}$$

$R(z)$ is the radius of the cylinder containing the whole jet, as defined in [37]. M_0 and $M_e(z)$ correspond respectively to the initial (at z=0) and the entrained mass flow rates from z_{min} to z, obtained from SPIV field measurements. Stereo-PIV measurements at the very close vicinity of the burner exit plane were quite delicate to perform mainly because of the laser light reflections on the burner exit throat surface. Consequently, stereo-PIV measurement start from z/D_b=0.12. The entrained masses are thus neglected for z/D_b ranging from 0 to 0.12. The axisymmetric assumption is verified using the transverse planes and the variability of the entrainment rate is assessed for different angular positions. Figure 13.a shows that the effect of the swirl intensity on the entrained ambient air quantities is weak. This is due probably to the return of the flow (which is included in the calculation of Me(z)) which increases with the swirl intensity. It is a kind of compensation between the global entrainment and the central

recirculation of the flow with the swirl intensity. It is noted that the Sn variation plays an important role on the CRZ compared to the entrainment. The effect of the air flow rate (Fig.13b), however, is relatively significant. When the airflow rate is multiplied by a factor of 3, the entrainment rate is increased by about 30% at a distance of 2.5 D_b from the burner.

Figures 14 (a) and (b) show respectively the influence of the oxygen enrichment and the equivalence ratio on the evolution of the entrainment rate along Z/D_b. We can note that the effects of these parameters remain relatively low. The entrainment rate Ψ globally decreases in reacting flow. Typically, it ranges from 1 to 0.6 for Z/D_b= 1.5 between the non-reactive and reactive cases. This is explained, on the one hand by a reduction in the density of entrained gases (burnt gases) and, on the other hand by an increase in the viscosity of the swirled jet in the reactive case. Figure 14 (b) shows that the normalized flame lift-off height H_{lo} increases from 0.7 to 1.5 with increasing the global equivalence ratio from 0.8 to 1. The results show that the entrainment rate increases linearly along the flow with a weak dependence on the global equivalence ratio. In particular, the entrainment rate slightly increases with increasing the global equivalence ratio at a given z/D_b position. These trends show that when the flame is stabilized further downstream, the mixture at the flame base is more diluted by surrounding gases, which are mainly composed of CO_2 and H_2O in a confined environment. This mechanism could lead to a decrease of flame temperature. A previous study [38] showed that NO_x emissions, via the thermal pathway, decrease with increasing the global equivalence ratio from 0.8 to 1. Therefore, the increase of entrained gases at the flame base with the global equivalence ratio could explain the NO_x emission trends. This induces a dilution of the reactive gases, which causes a reduction of flame temperature and consequently a reduction of NOx.

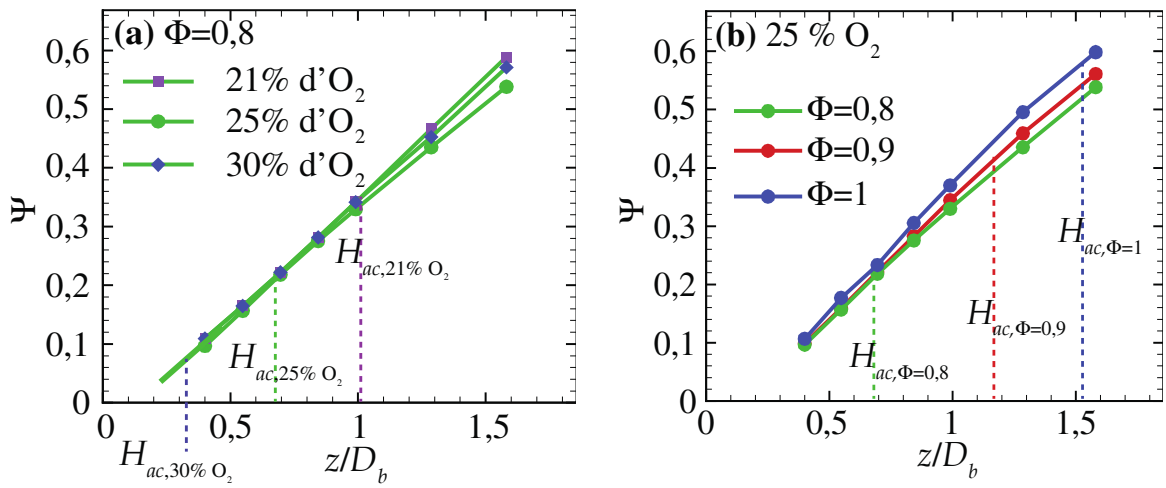

Fig. 14. Entrainment rate (ψ) as a function of z/D_b for the reacting flow: a) Effect O_2 enrichment (21, 25 and 30%) for the case S_{ng}=1.4 and Φ=0.8, b) Effect global equivalence ratio (0.8, 0.9 and 1) for the case S_{ng}=1,4 and 25% of O_2 .

3.6. Effects of O_2 enrichment on velocity fields

In this section, flow fields in reactive case when the oxygen enrichment in the oxidant varies from 21 to 30% of O_2 are compared. Figure 15 shows average fields (v_r, v_θ, v_z) for three O_2 contents 21, 25 and 30% for Φ = 0.8 and S_{ng} = 1.4 in the longitudinal plane of flow. The small white lines indicate the position of both sides of the flame base. The positions of the flame base (white lines) are used as an indication to show in which region of velocity the flame is stabilized. Before the point of stabilization the gases are fresh and after the gases are hot because we are in the post flame zone. These data were obtained by chemiluminescence on OH as shown in Figure 16 below. The most important information to extract from these data is that the flame stabilizes in areas of low longitudinal velocity (Fig.15, g-h-i); here, in the blue zone of the velocity fields (V_z between +1 and -1 m / s). Abel Inversion method to obtain a signal plane cannot not applied in this case because the configuration of the flow (rotating swirl in a given direction and radial fuel injection) is not axisymmetric. However, the flame base in our case is almost pointed on both sides (left and right), and therefore its

thickness is very small (1 to 2 mm), as illustrated in Figure 16. This makes it easy to determine the position of the flame base without the Abel Inversion method.

Oxygen enrichment in the oxidant (21 to 30%) moves the flame base to the burner outlet plane as it is shown in a previous paper [38]. This displacement of the reaction zone modifies the average velocity field as shown in Figure 15. With oxygen enrichment, the radial component is modified by a displacement of BGexp zones (Burned Gases in expansion) towards the burner as shown in Figures 15 (a), (b) and (c). These zones reflect the local expansion of the flue gases produced by the flame front. As the O_2 content of the oxidant increases, the flame temperature increases which induces a larger radial expansion. In addition, the volume of flame increases with the O_2 enrichment at constant Φ, which probably contributes to promote the radial expansion.

Figures 15 (d), (e) and (f) illustrate a decrease of the azimuthal component (v_θ) for the case of 30% O_2, whereas in the cases 21% and 25% of O_2, the azimuthal dynamic remains substantially the same. The bifurcation of azimuthal velocity zones occurs in the three cases of O_2 enrichment. It is observed further upstream in the flow when the O_2 content increases. We define the Central Stagnation Point (CSP) as the point at z/D_b minimum in the axis (r/D_b = 0) for which the axial velocity is zero. It moves upstream of the flow, from z/D_b=1.9 to 1.4 when the O_2 enrichment changes from 21 to 30% as shown in Figures 15 (g), (h) and (i). This evolution shows a reduction in size of the recirculation zone, which is a consequence of the approach of the reaction zone to the burner outlet plane.

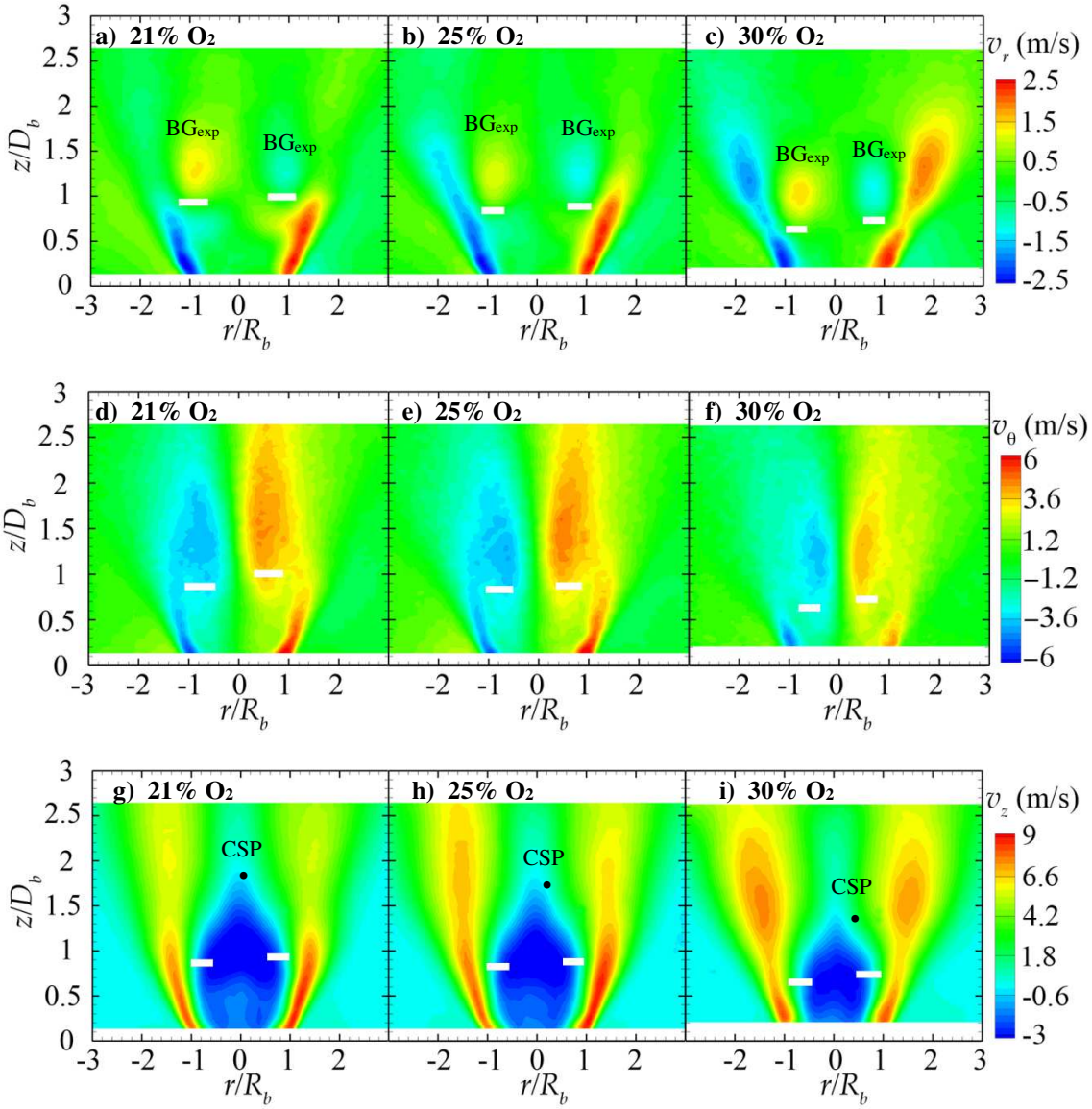

Fig. 15. Effect of O_2 enrichment (21, 25 and 30%) on the velocity fields in the longitudinal plane in reacting flow for S_{ng}=1.4 and Φ=0.8: a) b) c) radial velocity υ_r ; d) e) f) tangential velocity υ_θ; g) h) i) axial velocity υ_z. Small white lines show the position of the flame base.

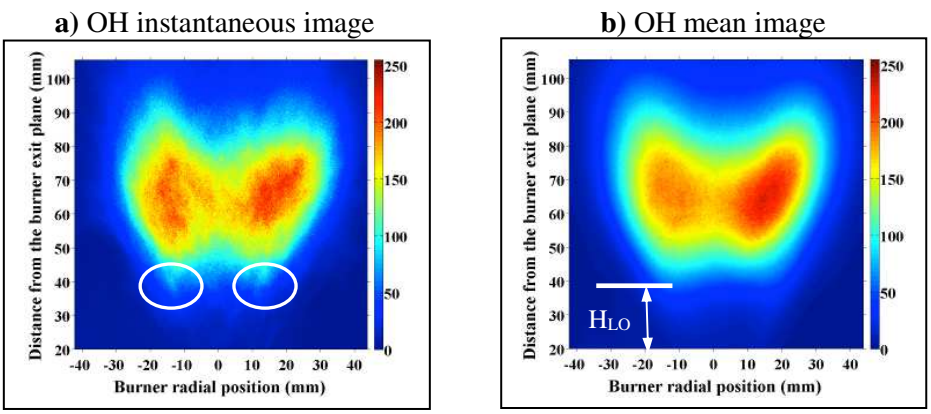

Fig. 16. Images of OH Chemiluminescence, flame case 21% of O_2 and Φ=0.8; a) Instantaneous and b) Mean images (H_{LO}: lift-off height).

3.7. Effects of equivalence ratio on velocity fields

In this section, flow fields in reactive case when the global equivalence ratio (Φ) changes from 0.8 to 1 are compared. Figure 16 presents the average fields (v_r, v_θ, v_z) for three Φ values (0.8, 0.9 and 1) at 25% of O and, S_{ng} = 1.4 in the longitudinal plane of the flow. We recall that the increase of Φ leads to a weak destabilization of the flame [38, 39] because the increase of dilution induced by the increase of recirculated CO_2 [38]. This is reflected in particular by an increase of the flame lift-off height and the associated fluctuations; but the flame remains generally stable and no blowout is observed. Figures 16 (a), (b) and (c) show that the radial expansion of the jet decreases as Φ increases from 0.8 to 1 for $z/D_b \leq 1.5$. When Φ = 1, the flame is stabilized at z/D_b=1.5 according to [38], which explains the radial expansion observed for these positions. It seems that the parameter Φ has little influence on the azimuthal velocity component as seen in Figures 16 (d), (e) and (f). With the evolution of Φ, a modification of the axial velocity component appears and more particularly in the region of the CRZ. The axial velocity of recirculation increases substantially as Φ increases as evidenced in Figure 15 (g), (h) and (i). The behavior of the CRZ is done in particular via the axial pressure gradient, which consequently seems to increase slightly when Φ increases with a greater decrease in the pressure as z decreases. The geometric shape of the CRZ is also modified when the global equivalence ratio evolves as shown in Figures 16 (g), (h) and (i).

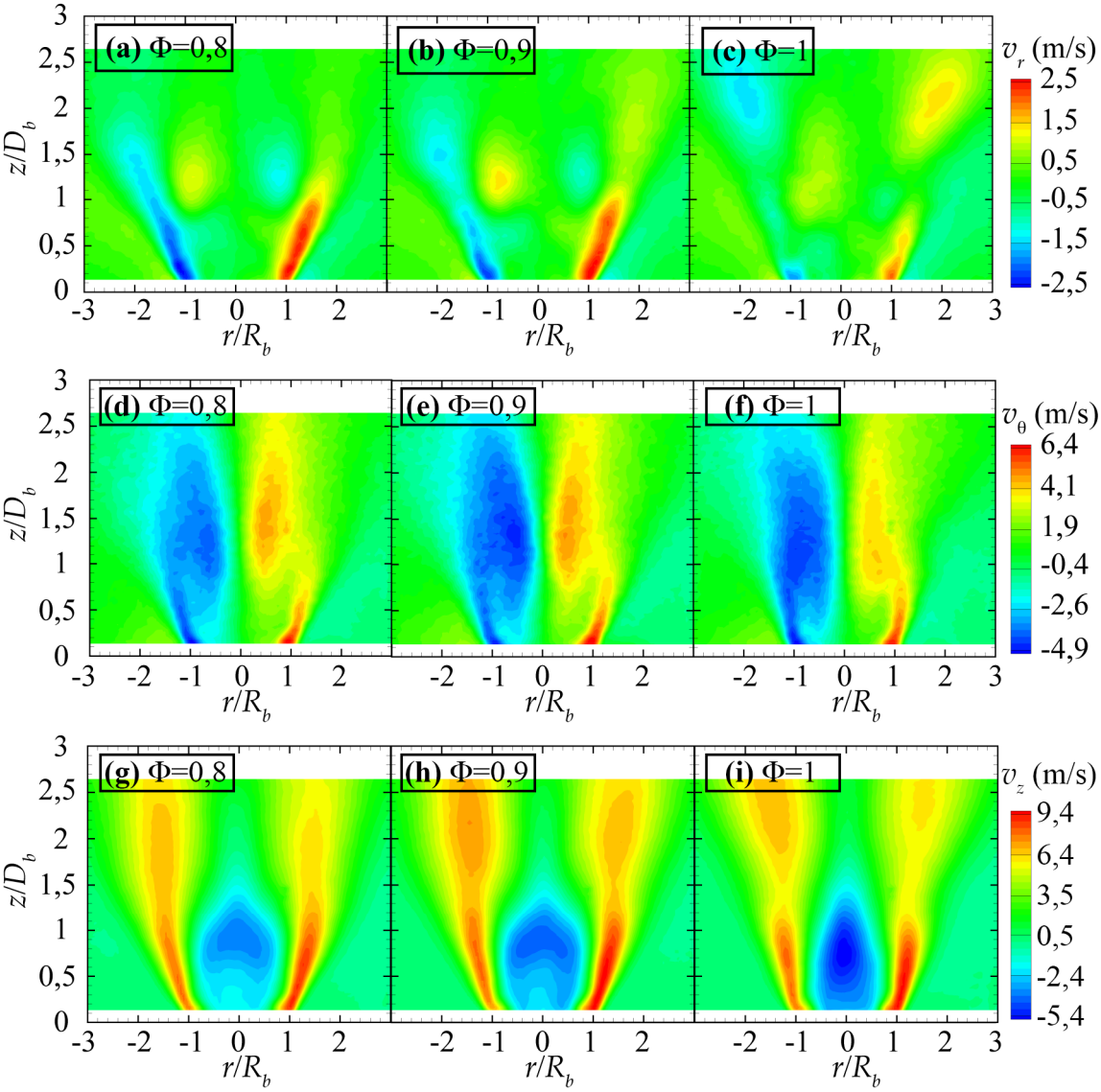

Fig. 16. Effect of the equivalence ratio (0.8, 0.9 and 1) on the velocity fields in the longitudinal plane in reacting flows S_{ng}=1.4 and 25% of O2: a) b) c) radial velocity υ_r ; d) e) f) tangential velocity υ_θ; g) h) i) axial velocity υ_z.

4. Conclusion

CH_4-air-O_2 turbulent swirling flames are investigated using stereo-PIV in reacting and non reacting conditions. The configuration of the burner is a coaxial one with a swirler in the annular part for the oxidizer and methane is injected radially through the central tube. Characteristics and topology of the flow are analyzed in the longitudinal and transverse planes throughout the 3D mean velocity fields, the turbulence intensity and the entrainment rate of surrounding gases. The swirling part of the flow and the central recirculation zone are clearly identified by Stereo-PIV measurements. Results show that the presence of the flame leads to a greater radial expansion of the jet in particular in the recirculation zone. Besides, the presence of the flame induces an increase of velocities downstream of the flow of because the rapid expansion of burned gases. In reactive case, the central recirculation zone (CRZ) is intensified and shows a bubble shape compared to the non-reactive case. The mean tangential velocity reveals a bifurcation of the maxima towards the jet central axis crossing the flame front. The tangential component of the turbulence intensity is amplified by the presence of the flame. Moreover, the turbulence intensity levels are higher at the top of the CRZ and in the vicinity of the jet central axis. The effective swirl number S_n is determined from stereo-PIV results and compared to the calculated geometrical swirl number $S_{ng.}$ The entrainment rate of surroundings gases along the flow is determined from measurements as a function of the swirl number and air the flow rate. The entrainment rate is also estimated for three global equivalence ratios in order to explain the decrease of NO_x (in Ref. 38) emissions with increasing the global equivalence ratio. The increase of the entrainment rate dilutes more the reactants, which decreases the flame temperature and consequently decreases NOx emissions. The O_2 enrichment moves the flame base closer to the burner and consequently modifies the average velocity field. Indeed, the velocity radial component is changed by a displacement of burned gases expansion zones closer to the burner, and the azimuthal component is decreased.

The central stagnation point (CSP) moves upstream of the flow when the O_2 enrichment increases. This behavior indicates a decrease in the size of the recirculation zone because the reaction zone is closer to the burner outlet.

Acknowledgments

The authors are grateful for the financial support of this work provided by the French Government's: ANR for the CO_2_EnergiCapt project (ANR-10-EESI-0003) and Investissement d'Avenir program: LABEX CAPRYSSES, under GrantANR-11-LABX-0006-01

References

[1] J.M. Beér, N.A. Chigier, Combustion Aerodynamics, Applied Sci. Publishers Ltd, (1972).

[2] A.K. Gupta, D.G. Lilley D.G, N. Syred, Swirl flows, Abacus Press (1984).

[3] S. Yuasa, Effects of swirl on the stability of jet diffusion flames, Combust. Flame, 66:181-92 (1986).

[4] D. Feikema, R.H. Chen, J.F. Driscoll, Blowout of nonpremixed flames: Maximum coaxial air velocities achievable, with and without swirl, Combust. Flame, 86:347-58(1991).

[5] S.F. Ahmed, R. Balachandran, T. Marchione, E. Mastorakos, Spark ignition of turbulent nonpremixed bluff-body flames, Combust. Flame, 151:366-85 (2007).

[6] Z. Mansouri, M. Aouissi, T. Boushaki, Numerical computations of premixed propane flame in a swirl stabilized burner: Effects of hydrogen enrichment swirl number and equivalence ratio on flame characteristics, International Journal of Hydrogen Energy, 41, 9664-9678 (2016).

[7] D. Galley, S. Ducruix, F. Lacas, D. Veynante, Mixing and stabilization study of a partially premixed swirling flame using laser induced fluorescence, Combust. Flame, 158:155-71 (2011).

[8] M. Stöhr, C.M. Arndt, W. Meier, Transient effects of fuel–air mixing in a partially-premixed turbulent swirl flame, Proc. Combust. Inst (2014).

[9] A.M. Steinberg, C.M. Arndt, W. Meier, Parametric study of vortex structures and their dynamics in swirl-stabilized combustion, Proc. Combust. Inst. 34, pp. 3117–3125(2013).

[10] Z. Mansouri, M. Aouissi, T. Boushaki**,** Detached eddy simulation of high turbulent swirling reacting flow in a premixed model burner, Combustion Science and Technology, Vol. 188, NOS. 11–12, 1777–1798 (2016).

[11] N. Syred, J.M. Béer, Combustion in swirling flows: A review, Combustion and Flame, 23:143-201(1974).

[12] P. Schmittel, B. Günther, B. Lenze, W. Leuckel, H .Bockhorn, Turbulent swirling flames: experimental investigation of the flow field and formation of nitrogen oxide, Proceedings of the Combustion Institute Volume 28, Issue 1, 2000, Pages 303-309.

[13] R.F. Huang, L.M. Duc, C.M. Hsu, Flow and mixing characteristics of swirling double-concentric jets influenced by a control disc at low central jet Reynolds numbers, International Journal of Heat and Fluid Flow, 00, 1–14 (2016).

[14] P. Jourdaine, C. Mirat, J. Caudal, A. Lo, T. Schuller, A comparison between the stabilization of premixed swirling CO2- diluted methane oxy-flames and methane/air flames, Fuel, (2016).

[15] A. C. Benim, S. Iqbal, W. Meier, F. Joos, A. Wiedermann, Numerical investigation of turbulent swirling flames with validation in a gas turbine model combustor, Applied Thermal Engineering, 110, 202–212 (2017).

[16] A.M. Elbaz, W.L. Robert, Investigation of the effects of quarl and initial conditions on swirling non-premixed methane flames: Flow field, temperature, and species distributions, Fuel 169, 120–134 (2016).

[17] E.E. Khalil Ahmed, K.A. Gupta, Towards distributed combustion for ultra low emission using swirling and non-swirling flowfields, Applied Energy 121, 132–139 (2014).

[18] R.C. Orbay, K.J. Nogenmyr, J. Klingmann, X.S. Bai, Swirling turbulent flows in a combustion chamber with and without heat release, Fuel 104, 133–146 (2013).

[19] S. Candel, D. Durox, T. Schuller, P. Palies, J.F. Bourgouin, J. Moeck, P. Jonas, Progress and challenges in swirling flame dynamics, C. R. Mecanique 340, 758–768 (2012).

[20] E. von Lavante, J. Yao, Numerical investigation of turbulent swirling flows in axisymmetric internal flow configurations, Flow Measurement and Instrumentation 25, 63–68 (2012).

[21] V. D. Milosavljevic, A. M. K. P. Taylor, J. H. Whitelaw, The influence of burner geometry and flow rates on the stability and symmetry of swirl stabilized nonpremixed flames, Combust. Flame 80 (2) 196-208 (1990).

[22] C. O. Iyogun; M. Birouk; J. A. Kozinski, Experimental investigation of the effect of fuel nozzle geometry on the stability of a swirling non-premixed methane flame, Fuel 90 (4), 1416-1423 (2011).

[23] F. Cozzi, A. Coghe, R. Sharma, Analysis of local entrainment rate in the initial region of isothermal free swirling jets by Stereo PIV, Experimental Thermal and Fluid Science 94 (2018) 281–294.

[24] A. Olivani. Thermo-fluid-dynamic Analysis of Methane/Hydrogen/Air Mixtures Under Reacting Conditions by Laser Diagnostics. PhD Thesis, Politecnico di Milano - Université d'Orléans, (2006).

[25] F. Cozzi, A. Coghe, Effect of air staging on a coaxial swirled natural gas flame, Experimental Thermal and Fluid Science 43 (2012) 32–39.

[26] P. Palies. “Dynamique et instabilités de combustion des flammes swirlées”. PhD Thesis, Ecole Centrale des Arts et Manufactures, (2010).

[27] T. Lieuwen, Unsteady Combustor Physics, Cambridge, (2012).

[28] T. Boushaki; J. C. Sautet; L. Salentey; B. Labegorre, The behaviour of lifted oxy-fuel flames in burners with separated jets, Int. Com. Heat Mass Transfer 34 (1) 8-18 (2007).

[29] N. Merlo, T. Boushaki, C. Chauveau, S. de Persis, L. Pillier, B. Sarh, I. Gökalp, Experimental Study of Oxygen Enrichment Effects on Turbulent Nonpremixed Swirling Flames, Energy Fuels, 27 (10) 6191-6197(2013).

[30] H. S. Zhen; C. W. Leung; C. S. Cheung, Combustion characteristics of a swirling inverse diffusion flame upon oxygen content variation, Applied Energy 88 (9), 2925-2933 (2011).

[31] P. Bělohradský; P. Skryja; I. Hudák, Experimental study on the influence of oxygen content in the combustion air on the combustion characteristics, Energy 75, 116-126 (2014).

[32] T. Boushaki, A. Koched, Z. Mansouri, F. Lespinasse, Volumetric velocity measurements (V3V) on turbulent swirling flows, Flow Measurement and Instrumentation, Volume 54, 46-55 (2017).

[33] N. Merlo, T. Boushaki, C. Chauveau, S. de Persis, L. Pillier, B. Sarh, and I. Gökalp, Combustion characteristics of methane-oxygen enhanced air turbulent non-premixed swirling flames, Experimental Thermal and Fluid Science, 56, 53–60 (2014).

[34] Z. Mansouri, T. Boushaki, Experimental and numerical investigation of turbulent isothermal and reacting flows in a non-premixed swirl burner, International Journal of Heat and Fluid Flow, Vol. 72, (2018), Pages 200–213.

[35] N.A. Chigier, A. Chervinsky, Experimental Investigation of Swirling Vortex Motion in Jets, Journal of Applied Mechanics, 34:443-51(1967).

[36] D. Durox, J.P. Moeck, J.F. Bourgouin, P. Morenton, M. Viallon, T. Schuller, S. Candel, Flame dynamics of a variable swirl number system and instability control, Combust. Flame, 160:1729-42 (2013).

[37] S.C. Crow, F.H; Champagne, Orderly structure in jet turbulence, J. Fluid Mech. 48:547-91(1971).

[38] T. Boushaki, N. Merlo, C. Chauveau, I. Gökalp, Study of pollutant emissions and dynamics of non-premixed turbulent oxygen enriched flames from a swirl burner, Proc. Comb. Inst. 36:3959–3968 (2017).

[39] H. Zaidaoui, T. Boushaki, J. C. Sautet, C. Chauveau, B. Sarh & I. Gökalp, Effects of CO_2 Dilution and O_2 Enrichment on Non-premixed Turbulent CH4-Air Flames in a Swirl Burner, Combustion Science and Technology, Vol. 190, Is 5, p 784-802 (2018).

[40] T. Boushaki; J. C. Sautet; B. Labegorre, Control of flames by radial jet actuators in oxy-fuel burners, Combustion and Flame 156, 2043–2055 (2009).

[41] T. Takagi, H.D. Shin, A. Ishio, Properties of turbulence in turbulent diffusion flames, Combustion and Flame, 40, 121-140 (1981).